

MDPI

Article

# Electrocatalytic and Conductive Vanadium Oxide on Carbonized Bacterial Cellulose Aerogel for the Sulfur Cathode in Li-S Batteries

Xueyan Lin <sup>1</sup>, Wenyue Li <sup>2</sup>, Xuan Pan <sup>3</sup>, Shu Wang <sup>4</sup> and Zhaoyang Fan <sup>2</sup>,\*

- School for Engineering of Matter, Transport & Energy, Arizona State University, Tempe, AZ 85281, USA
- School of Electrical, Computer and Energy Engineering, Arizona State University, Tempe, AZ 85281, USA
- <sup>3</sup> Institutes of Science and Development, Chinese Academy of Sciences, Beijing 100190, China
- College of Health Solutions, Arizona State University, Phoenix, AZ 85004, USA
- \* Correspondence: zhaoyang.fan@asu.edu

Abstract: Many transition-metal-oxide-based catalysts have been investigated to chemically bind soluble lithium polysulfides and accelerate their redox kinetics in lithium-sulfur (Li-S) battery chemistry. However, the intrinsic poor electrical conductivities of these oxides restrict their catalytic performance, consequently limiting the sulfur utilization and the rate performance of Li-S batteries. Herein, we report a freestanding electrocatalytic sulfur host consisting of hydrogen-treated  $VO_2$  nanoparticles (H-VO<sub>2</sub>) anchored on nitrogen-doped carbonized bacterial cellulose aerogels (N-CBC). The hydrogen treatment enables the formation and stabilization of the rutile  $VO_2(R)$  phase with metallic conductivity at room temperature, significantly enhancing its catalytic capability compared to the as-synthesized insulative  $VO_2(M)$  phase. Several measurements characterize the electrocatalytic performance of this unique H-VO<sub>2</sub>@N-CBC structure. In particular, the two kinetic barriers between  $S_8$ , polysulfides, and  $Li_2S$  are largely reduced by 28.2 and 43.3 kJ/mol, respectively. Accordingly, the Li-S battery performance, in terms of sulfur utilization and charge/discharge rate, is greatly improved. This work suggests an effective strategy to develop conductive catalysts based on a typical transition metal oxide ( $VO_2$ ) for Li-S batteries.

Keywords: lithium-sulfur battery; hydrogenated VO<sub>2</sub>; electrocatalysts; free-standing cathode



Citation: Lin, X.; Li, W.; Pan, X.; Wang, S.; Fan, Z. Electrocatalytic and Conductive Vanadium Oxide on Carbonized Bacterial Cellulose Aerogel for the Sulfur Cathode in Li-S Batteries. *Batteries* **2023**, *9*, 14. https://doi.org/10.3390/ batteries9010014

Academic Editors: Pascal Venet, Karim Zaghib and Seung-Wan Song

Received: 14 November 2022 Revised: 15 December 2022 Accepted: 22 December 2022 Published: 26 December 2022



Copyright: © 2022 by the authors. Licensee MDPI, Basel, Switzerland. This article is an open access article distributed under the terms and conditions of the Creative Commons Attribution (CC BY) license (https://creativecommons.org/licenses/by/4.0/).

# 1. Introduction

As one of the emerging energy storage devices, lithium-sulfur (Li-S) batteries are attracting considerable interest due to their high theoretical energy density (2600 Wh kg<sup>-1</sup>) and specific capacity (1672 mAh/g), as well as the abundance of low-cost sulfur sources [1]. However, the highly insulating nature of S and Li<sub>2</sub>S that causes poor sulfur utilization and large polarization, along with the severe shuttle effect of lithium polysulfides (LiPSs) that results in rapid capacity degradation and poor cycle life, critically impede the commercialization of Li-S batteries. Many studies have been conducted to construct conductive sulfur host materials and structures to resolve these problems [2]. Coupling sulfur with porous nanocarbons (e.g., aerogels, hollow spheres, graphene and carbon nanotubes) is a common strategy to simultaneously improve cathode electrical conductivity and physically confine dissolved LiPSs in the porous structure [3–7]. Furthermore, chemical modification of the nonpolar carbon host to form a polar surface by heteroatom doping vastly enhances its interactions with polar LiPSs, consequently alleviating the shuttle effect [8–12]. The sluggish redox reaction kinetics of LiPSs leads to their concertation accumulation in the electrolyte around the cathode region, accelerating the diffusion and migration of LiPSs toward the Li anode [13]. Therefore, electrocatalysts that capture and accelerate the redox reactions of LiPSs have attracted enormous attention. This category of materials consists of transition metal oxides, nitrides, and sulfides, among others [3,14–20].

Batteries 2023, 9, 14 2 2 of 13

Of the various metal compounds, oxides have a higher binding capability to LiPSs than their nitrides and sulfides counterparts but suffer from their more insulative nature that severely restricts their overall catalytic behavior [21,22]. For these oxides with low conductivity, the electrocatalytic reaction process of LiPSs involves three primary steps: adsorption on the electrocatalyst surface, diffusion to the neighboring conductive surface to accept (or donate) electrons and Li<sup>+</sup> ions, and the subsequent redox conversion. The necessary strong binding between LiPSs and the catalyst essentially prevents LiPSs from diffusion on the catalyst surface and therefore suffocates the whole process [23]. An ideal polysulfide electrocatalyst must also be electronically conductive in addition to its appropriate adsorption capability to immobilize LiPSs and catalytic activity to accelerate polysulfide conversion [24]. A few conductive oxides, such as hydrogen-reduced  $TiO_{2-x}$  [25] and  $Ti_4O_7$  [26] and nitride/oxide composites [27], have been reported with excellent catalytic performance in Li-S chemistry.

Among the many polymorph phases of  $VO_2$ ,  $VO_2(R)$  and  $VO_2(M)$  are stable phases at high and low temperatures, respectively. The rutile  $VO_2(R)$  phase is a metallic conductor with a conductivity of  $\sim 10^4$  S/cm, rendering it a suitable electrocatalyst for polysulfides. However, this high-temperature stable phase experiences a metal-insulator transition at  $\sim 68$  °C in the low-temperature monoclinic  $VO_2(M)$  phase, which is electrically insulative with a conductivity of less than 0.1 S/cm $^{-1}$  [28]. Fortunately, studies have shown that hydrogen doping stabilizes metallic  $VO_2(R)$  below room temperatures [29–32]. Our previous study showed that changing the stoichiometry of  $VO_2$  or doping protons into  $VO_2$  using  $VO_2$  treatment can substantially increase its electrical conductivity [33].

Herein, we report our study on conductive VO<sub>2</sub> nanoparticles (NPs) as the electrocatalyst in Li-S chemistry. To our knowledge, this is the first report of exploiting the conductive rutile VO<sub>2</sub>(R) phase as the electrocatalyst to accelerate the polysulfide conversion reaction in Li-S batteries. We synthesized H<sub>2</sub> thermal-treated VO<sub>2</sub> NPs anchored on N-doped carbonized bacterial cellulose (H-VO<sub>2</sub>@N-CBC) to overcome the insulating problem of the oxide catalysts and to modify the carbon scaffold surface. N-doped carbonized bacterial cellulose has been proven to be an excellent freestanding sulfur host [34]. CBC surface modification by N-dopants and H-VO<sub>2</sub> NPs can also improve electrolyte wettability, facilitating a better charge transfer [35]. N-dopants on the CBC surface could further serve as active sites for VO<sub>2</sub> NP nucleation and growth [36]. The highly conductive H-VO<sub>2</sub> NPs catalyze the Li-S redox reactions and regulate Li<sub>2</sub>S and S<sub>8</sub> deposition. With this H-VO<sub>2</sub>@N-CBC structure as the sulfur host, we studied its electrocatalytic functions through several electrochemical characterizations. In particular, the two kinetic barriers between  $S_8$ , polysulfides, and Li<sub>2</sub>S are significantly reduced by 28.2 and 43.3 kJ/mol, respectively, compared to the N-CBC-based structure. Accordingly, the Li-S battery performance, in terms of sulfur utilization and charge/discharge rate, is significantly improved.

#### 2. Materials and Methods

#### 2.1. Material Synthesis

The nitrogen-doped carbonized bacterial cellulose (N-CBC) matrix was prepared by carbonization of the freeze-dried BC aerogel at 900 °C under an Ar atmosphere with the assistance of urea. The freestanding VO<sub>2</sub>-NP-decorated N-doped CBC (VO<sub>2</sub>@N-CBC) composite was fabricated via a solvothermal method. In brief, 265 mg Vanadyl Acetylacetonate (VO(acac)<sub>2</sub>) was first dissolved in ethanol (95 mL) and kept stirring for 24 h, during which the V<sup>5+</sup> was reduced to V<sup>4+</sup>. Afterward, the solution was transferred into a Teflon-lined stainless-steel autoclave with 50 mg N-CBC and 5 mL DI water added. After heating at 180 °C for 24 h, the obtained VO<sub>2</sub>@N-CBC was rinsed with DI water and ethanol several times and dried in an oven at 80 °C. The dried VO<sub>2</sub>@N-CBC sheet was treated at 450 °C for 2 h under a 5% H<sub>2</sub>/Ar mixed atmosphere to obtain the final H-VO<sub>2</sub>@N-CBC sample. Then, the samples were punched into a disk with a diameter of 12 mm, which served as the freestanding sulfur hosts.

Batteries 2023, 9, 14 3 of 13

#### 2.2. Material Characterization

The scanning electron microscopy (SEM) images of the prepared nanostructured samples were acquired using Zeiss Auriga at an acceleration voltage of 5 kV. The powder X-ray diffraction (XRD) measurements were performed on an X-ray Diffractometer (Malvern PANalytical Aeris) with Cu K $\alpha$  radiation ( $\lambda=0.1541$  nm) over the  $2\theta$  range of  $10\text{--}80^\circ$  with a scan speed of  $2^\circ$  min $^{-1}$  at room temperature. The X-ray photoelectron spectroscopy (XPS) spectra were recorded by a Krator Axis Supra + apparatus using Al K-alpha (1486.6 eV) as the excitation light source.

#### 2.3. Electrochemical Measurement

Lithium polysulfide adsorption tests:  $0.25~M~Li_2S_6$  solution was first prepared by mixing sublimed sulfur powder and Li<sub>2</sub>S with a molar ratio of 5:1 in blank electrolyte, which consists of 1 M bis(trifluoroethanesulfonyl)imide lithium (LiTFSI), 2 wt% lithium nitrites (LiNO<sub>3</sub>) in 1.3-dioxolane (DOL) and 1.2-dimethoxy ethane (DME) (1:1, v/v) solution. The 0.25 M Li<sub>2</sub>S<sub>6</sub> solution was then diluted to 0.05 M for the visual adsorption test. 1.13 m<sup>2</sup> of each sample, H-VO<sub>2</sub>@N-CBC, VO<sub>2</sub>@N-CBC and N-CBC, was loaded into 4 mL 0.05 M Li<sub>2</sub>S<sub>6</sub> solution to observe the color change. All samples were vacuum-dried at 80 °C overnight before testing.

Assembly of Li<sub>2</sub>S<sub>6</sub> symmetric cells and their cyclic voltammogram (CV) measurement: Two identical electrodes with the same materials were used as working and counter electrodes, and 40  $\mu$ L 0.25 M Li<sub>2</sub>S<sub>6</sub> catholyte was dropped on each electrode. The CV of these symmetric cells was measured at a scan rate of 3 mV s<sup>-1</sup> and 10 mV s<sup>-1</sup> with a potential window between -1 and 1 V to evaluate the polysulfide conversion kinetics.

 $\rm Li_2S$  precipitation test: Nucleation and growth of  $\rm Li_2S$  on three different electrodes were conducted by dropping 20  $\mu L$  0.25 M  $\rm Li_2S_8$  catholyte on each electrode and another 20  $\mu L$  blank electrolyte on the Li-chip anode side. The assembled cells were first to galvano-statically discharged at 0.1 mA/g to 2.06 V and then potentiostatically discharged at 2.05 V for  $\rm Li_2S$  precipitation and growth until the current dropped below  $10^{-5}$  A.

Li-S coin cell battery assembly and electrochemical performance: The H-VO<sub>2</sub>@N-CBC/S, VO<sub>2</sub>@N-CBC/S, and N-CBC/S composite cathodes were prepared by dropping 60  $\mu$ L 0.25 M Li<sub>2</sub>S<sub>6</sub> catholyte on each electrode to obtain a sulfur loading of 2.5 mg cm<sup>-2</sup>. CR 2016 coin cells were assembled in an argon-filled glove box using the prepared H-VO<sub>2</sub>@N-CBC/S, VO<sub>2</sub>@N-CBC/S and N-CBC/S composite cathodes, Celgard 2400 membranes as the separators, and lithium chip as the anode. The galvanostatic charge–discharge curves of these Li-S cells were recorded on a LANDCT2001A battery test under different current rates at a voltage range from 1.7 to 2.8 V. Their CV profiles were collected on a Biologic SP-240 electrochemical workstation at a scan rate from 0.2 to 0.5 mV s<sup>-1</sup>. The electrochemical impedance spectrum (EIS) was collected in the range of 100 kHz–0.01 Hz with an AC voltage amplitude of 5 mV.

## 3. Results

## 3.1. Material Characterization

Figure 1a schematically shows the cathode scaffold fabrication process. BC aerogel, derived from BC hydrogel after freeze-drying, is carbonized with urea in an Ar environment to obtain N-doped carbon nanofiber aerogel (N-CBC). Through a solvothermal process,  $VO_2$  nanoparticles (NPs) are grown on N-CBC, which is further thermally treated in a  $H_2/Ar$  environment to convert the insulating  $VO_2$  to its conductive form, called H-VO<sub>2</sub> here. The SEM images in Figure 1b,c show the microscopic morphology of  $VO_2@N$ -CBC and H-VO<sub>2</sub>@N-CBC, respectively, revealing that the oxide NPs are anchored on the carbon nanofibers. The whole structure is well connected to form a 3D scaffold for the rapid transportation of electrons and  $Li^+$  ions and for hosting sulfur species.

Batteries 2023, 9, 14 4 of 13

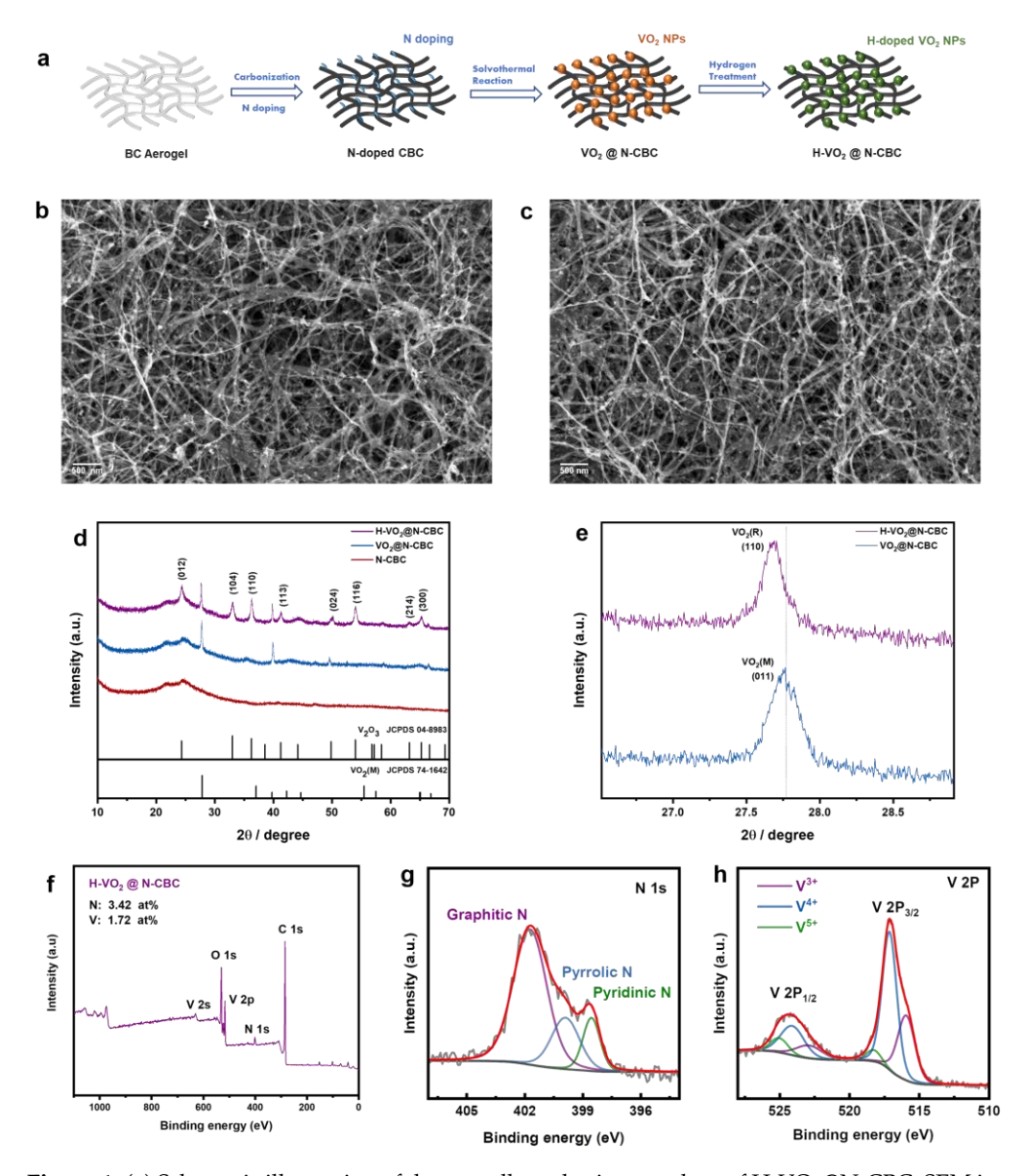


**Figure 1.** (a) Schematic illustration of the overall synthesis procedure of H-VO<sub>2</sub>@N-CBC; SEM images of (b) VO<sub>2</sub>@N-CBC and (c) H-VO<sub>2</sub>@N-CBC; (d) XRD pattern of H-VO<sub>2</sub>@N-CBC, VO<sub>2</sub>@N-CBC, and N-CBC, and (e) a magnified region of the XRD data in  $26^{\circ} \leq 2\theta \leq 29^{\circ}$ ; (f) XPS broad survey and high-resolution (g) N 1 s and (h) V 2 p spectra of H-VO<sub>2</sub>@N-CBC.

The crystal structures and phase transitions of the prepared samples were studied using the X-ray diffraction (XRD) technique, as presented in Figure 1d. The XRD patterns of N-CBC mainly display a broad peak in the range of 20–30°, indicating an amorphous nature of the carbonized aerogels [37] because the carbonization was conducted at a limited temperature of 900 °C. However, the prepared VO<sub>2</sub>@N-CBC presents two prominent diffraction peaks at 27.8° and 39.8°, corresponding to the (0 1 1) and (0 2 0) planes of the VO<sub>2</sub>(M) phase (JCPDS No. 074-1642), respectively. After hydrogen treatment, these two dominant VO<sub>2</sub> characteristic peaks were retained at similar diffraction angles, but additional peaks appear at 24.3°, 33.0°, 36.3°, 41.2°, 49.9°, 53.9°, 63.2° and 65.2°, which are indexed to the (0 1 2), (1 0 4), (1 1 0), (1 1 3), (0 2 4), (1 1 6), (2 1 4) and (3 0 0) reflections of V<sub>2</sub>O<sub>3</sub> (JCPDS No. 005-4280), respectively. The formation of V<sub>2</sub>O<sub>3</sub> reveals that partial VO<sub>2</sub>(M) was reduced during the hydrogen annealing and carbothermal reduction processes [33]. It is noted that V<sub>2</sub>O<sub>3</sub> has a conductivity of ~10<sup>3</sup> S/cm [38], while VO<sub>2</sub>(M) is insulative with a conductivity of ~0.1 S/cm.

Batteries 2023, 9, 14 5 of 13

A careful inspection reveals that the two preserved VO<sub>2</sub>-related peaks, in fact, slightly shift to a lower diffraction angle: from 27.8° to 27.6° (Figure 1e) and from 39.8° to 39.7°, respectively, and these two new peaks can be ascribed to the (1 1 0) and (2 0 0) planes of the  $VO_2(R)$  phase [29,31,39]. It is well known that the high-temperature  $VO_2(R)$  phase is a metallic conductor with a conductivity of ~10<sup>4</sup> S/cm, which experiences metal-insulator transition at  $\sim$ 68  $^{\circ}$ C to the low-temperature insulative VO<sub>2</sub>(M) phase [28]. However, studies have shown that hydrogen doping stabilizes metallic VO<sub>2</sub>(R) at low temperatures [29,30]. From the XRD peak position shift measured at room temperature and the appearance of the  $V_2O_3$  phase, we consider that our H-VO<sub>2</sub>@N-CBC sample consists of metallic VO<sub>2</sub>(R) and V<sub>2</sub>O<sub>3</sub> phases. During hydrogen thermal treatment, VO<sub>2</sub> was in its metallic rutile phase. When the temperature cooled down, the metallic phase was maintained with hydrogen dopants with no transition to the insulating VO<sub>2</sub>(M) monoclinic phase. This inference was corroborated by the observation that the synthesized pure VO<sub>2</sub> powder's conductance measured at 100 °C is a few orders larger than that measured at room temperature. In contrast, after the hydrogen thermal treatment, its conductance at room temperature becomes similar to that at high temperatures. The resultant V<sub>2</sub>O<sub>3</sub> /VO<sub>2</sub>(R) mixed phases possess metallic conductivity at room temperature compared to the initial insulating VO<sub>2</sub>(M) phase, which can remarkably facilitate electron and ion transport [31,33,40].

The chemical configuration and oxidation states of H-VO<sub>2</sub>@N-CBC were investigated using X-ray photoelectron spectroscopy (XPS). The broad survey shown in Figure 1f reveals the presence of C, N, V and O elements. The atomic percentages of N and V were detected to be 3.42 at % and 1.72 at %, respectively. The high-resolution V 2p spectra presented in Figure 1h show a typical doublet profile of V  $2p_{3/2}$  and V  $2p_{1/2}$ , and each can be deconvoluted into three peaks. Two prominent peaks located at 517 and 524 V are ascribed to the  $V^{4+}$  oxidation states, whilst the two peaks at 515.8 and 522.8 V are assigned to the  $V^{3+}$ oxidation states, indicating the partial reduction from  $V^{4+}$  to  $V^{3+}$  [41]. The two small peaks corresponding to  $V^{5+}$  are due to unavoidable surface oxidation in the air [42]. In general,  ${
m V}^{4+}$  was found to be the dominating oxidation state in the vanadium oxide mixture, at least on the surface. Regarding the N 1s high-resolution spectra in Figure 1g, peaks at 398.6, 400.1, and 401.3 eV refer to pyridinic N, pyrrolic N, and graphitic N, respectively [43,44]. The existence of N species confirms that N dopants have been successfully incorporated into CBC nanofibers. Furthermore, the main graphitic-N species, which affect the electronic and geometric structure of carbon, can increase conductivity and promote electron transfer [45,46].

## 3.2. Polysulfide Binding and Li<sub>2</sub>S Precipitation

A strong binding to the electrocatalyst surface is essential for LiPSs to expedite their redox reactions. To evaluate the adsorption ability of H-VO<sub>2</sub>@N-CBC, VO<sub>2</sub>@N-CBC and N-CBC, the three freestanding scaffolds were placed into the diluted Li<sub>2</sub>S<sub>6</sub> solution (0.005 M) and kept still for 12 h for observation as shown in Figure 2a. The dark yellow Li<sub>2</sub>S<sub>6</sub> solution became completely colorless after 12 h for H-VO<sub>2</sub>@N-CBC. The visual test reveals that the polysulfide adsorption ability follows the sequence of H-VO<sub>2</sub>@N-CBC > VO<sub>2</sub>@N-CBC > N-CBC. In N-CBC, its N-dopants and porous structure contribute to the adsorption of polysulfides [34]. By incorporating a small amount of VO<sub>2</sub> NPs in VO<sub>2</sub>@N-CBC, more polysulfides are absorbed due to the chemical capturing effect of VO<sub>2</sub> NPs [47]. However, the color of the solutions only became clear for H-VO<sub>2</sub>@N-CBC. Oxygen vacancies in metal oxides have been regarded as the active sites for the chemical adsorption of polysulfide [48]. The more vital adsorption ability of H-VO<sub>2</sub> than VO<sub>2</sub> suggests that the hydrogen/carbon thermal treatment substantially promotes the generation of oxygen vacancies in H-VO<sub>2</sub>, facilitating its binding with polysulfides.

Batteries 2023, 9, 14 6 of 13

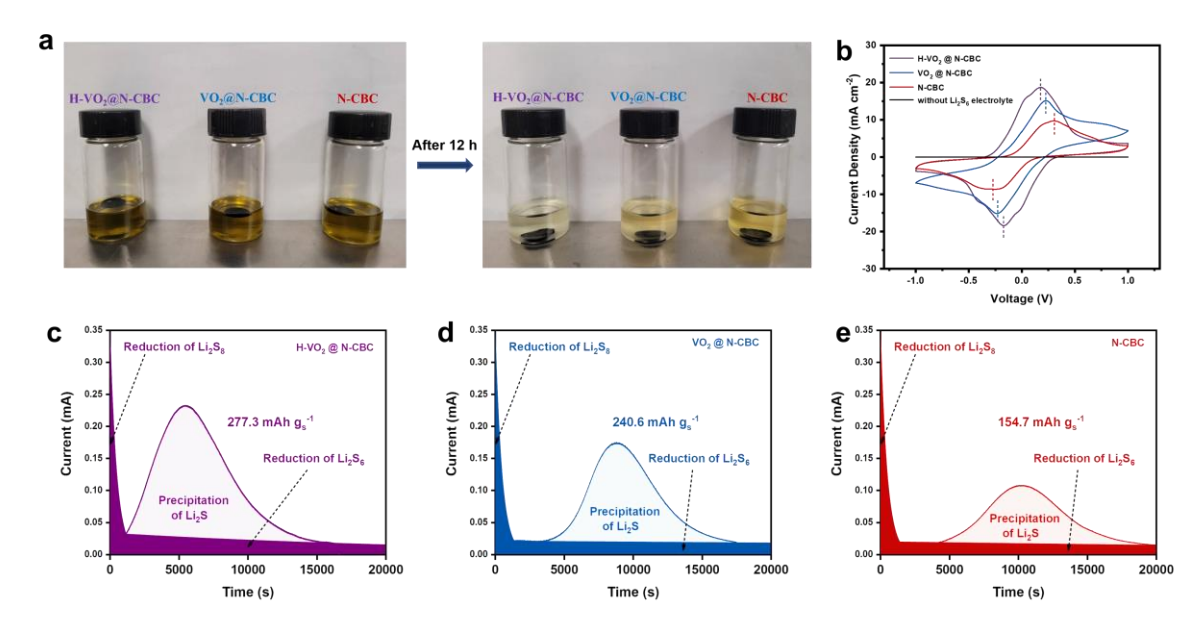


**Figure 2.** (a) Photos of H-VO<sub>2</sub>@N-CBC, VO<sub>2</sub>@N-CBC, and N-CBC initially added in 5 mM Li<sub>2</sub>S<sub>6</sub> solution and after aging for 12 h; (b) cyclic voltammetry (CV) curves of Li<sub>2</sub>S<sub>6</sub> symmetric cells with H-VO<sub>2</sub>@N-CBC, VO<sub>2</sub>@N-CBC, and N-CBC electrodes at a scan rate of 10 mV/s; Li<sub>2</sub>S precipitation process of (c) H-VO<sub>2</sub>@N-CBC, (d) VO<sub>2</sub>@N-CBC, and (e) N-CBC under potentiostatic discharge conditions.

To assess the catalytic ability of the three types of sulfur host in promoting polysulfide conversion, we first characterized the  $\text{Li}_2\text{S}_6$  symmetric cells using cyclic voltammetry (CV). When the symmetric cells were tested at the scan rate of 10~mV/s, as shown in Figure 2b, the H-VO2@N-CBC electrode displayed the smallest polarization (voltage gap between cathodic and anodic peaks) and the highest peak current density among the three samples for the polysulfide redox transformation. The CV curves of the VO2-based electrodes (H-VO2@N-CBC and VO2@N-CBC) with  $\text{Li}_2\text{S}_6$  electrolyte clearly exhibited two pairs of reversible redox peaks after slowing down the scan rate to 3~mV/s as shown in Figure S1a,b, labeled as peaks a, b, c and d. At the same time, the N-CBC shown in Figure S1c still presents only one pair of redox peaks. It is generally considered that peak a represents the oxidation of  $\text{Li}_2\text{S}$  to LiPSs, and peak b suggests the formation of  $\text{S}_8$  from LiPSs, while the other two peaks c and d are the reversible processes of peaks b and a, respectively [49]. Without  $\text{Li}_2\text{S}_6$  presenting in the electrolyte, all these samples showed no apparent reactions. This result suggests that H-VO2@N-CBC had the best performance.

We then investigated the kinetics of Li<sub>2</sub>S nucleation and growth to further evaluate the polysulfide conversion ability of the three types of electrodes. For this measurement, the potentiostatic discharge profiles at 2.05 V of the cells for the three types of electrodes were collected. It was observed, according to Figure 2c-e, that the time-current curves first sharply decreased due to the reduction of Li<sub>2</sub>S<sub>8</sub> followed by an increase in the current representing the onset of Li<sub>2</sub>S nucleation. Subsequently, the current reached its peak and then gradually dropped, corresponding to the impingement between Li<sub>2</sub>S nuclei that led to the ending of the Li<sub>2</sub>S phase growth. The background current intensity can be attributed to the reduction of Li<sub>2</sub>S<sub>6</sub>. By calculating the integrated area of the charge flow, the capacity released from Li<sub>2</sub>S precipitation can be obtained [50]. As shown in Figure 2c–e, the responsiveness of Li<sub>2</sub>S nucleation is earlier on H-VO<sub>2</sub>@N-CBC than on VO<sub>2</sub>@N-CBC and N-CBC. Moreover, H-VO<sub>2</sub>@N-CBC exhibited the highest current (0.195 mA) and capacity  $(277.3 \text{ mAh g}^{-1})$  for the Li<sub>2</sub>S precipitation process compared to VO<sub>2</sub>@N-CBC (0.174 mA, 240.6 mAh  $g^{-1}$ ) and N-CBC (0.106 mA, 154.7 mAh  $g^{-1}$ ). Corroborating the above CV study, these results show that H-VO<sub>2</sub>@N-CBC features the best capability to promote Li<sub>2</sub>S precipitation and consequently enable the efficient utilization of lithium polysulfides [51].

Batteries 2023, 9, 14 7 of 13

### 3.3. Activation Energy Barriers

We assembled Li-S full cells using the three types of sulfur host and investigated their catalytic functions by measuring the reaction kinetic barriers. The CV profiles of these cells at a scan rate of 0.2 mV/s are presented in Figure 3a. In the cathodic scan, the first peak voltages of 2.295, 2.267 and 2.223 V were observed for the H-VO<sub>2</sub>@N-CBC, VO<sub>2</sub>@N-CBC and N-CBC electrodes, respectively, which corresponded to the reaction from S<sub>8</sub> to polysulfide (S<sub>8</sub> -> Li<sub>2</sub>S<sub>n</sub>). Afterward, the second peak voltages referring to the conversion from polysulfide to Li<sub>2</sub>S (Li<sub>2</sub>S<sub>n</sub> -> Li<sub>2</sub>S) in the cathodic scan were 1.977, 1.957 and 1.879 V for the H-VO<sub>2</sub>@N-CBC, VO<sub>2</sub>@N-CBC and N-CBC electrodes, respectively. Correspondingly, the anodic peaks can be attributed to the oxidation of Li<sub>2</sub>S toward soluble Li<sub>2</sub>S<sub>n</sub> and sulfur. For H-VO<sub>2</sub>@N-CBC, the cathodic peaks shift to a higher potential, and the anodic peaks shift to a lower potential compared to the peaks of the VO<sub>2</sub>@N-CBC and N-CBC cathodes. The smallest peak voltage separation between the cathodic and anodic peaks as well as the highest exchange current density indicate the enhanced redox kinetics of H-VO<sub>2</sub>@N-CBC [52].

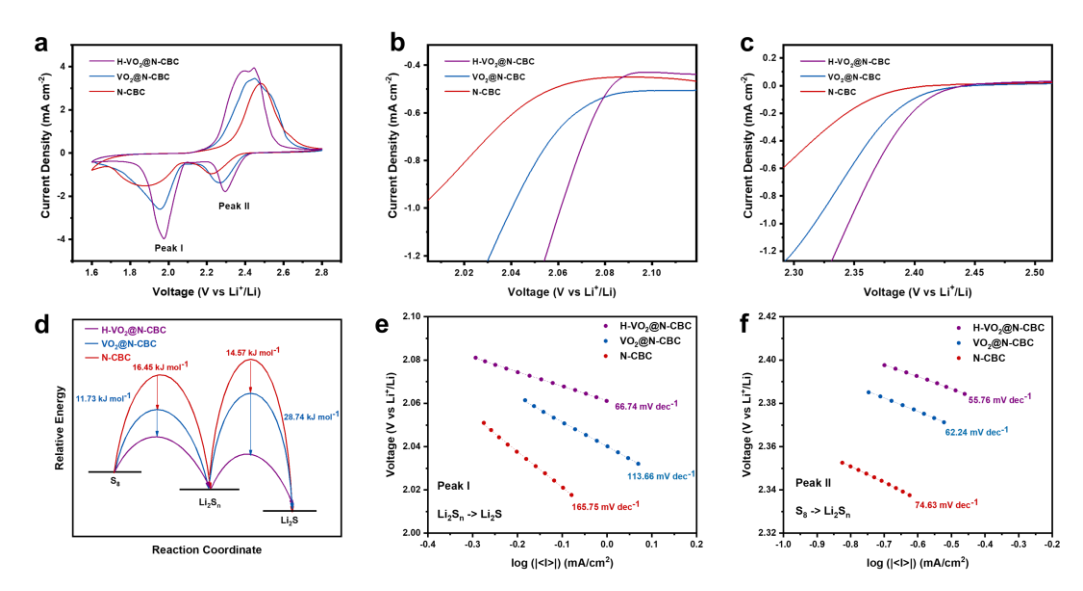


**Figure 3.** (a) Cyclic voltammetry (CV) profiles of the Li-S cells with H-VO<sub>2</sub>@N-CBC-, VO<sub>2</sub>@N-CBC- and N-CBC-based cathodes at a scan rate of 0.2 mV/s with the voltage range of 1.6~2.8 V; (b,c) linear sweep voltammetry (LSV) curves obtained from Figure 3a near Peak I and Peak II; (d) relative activation energy difference among three electrodes depending on a reaction coordinate; (e,f) the corresponding Tafel plot derived from the LSV curves in Figure 3b,c for Peak I and Peak II.

To quantitively verify the catalytic effect of H-VO<sub>2</sub> and VO<sub>2</sub> NPs, the relative activation energy for each reaction step in the discharge process was estimated using the equation  $E_a = E_a^0 - \frac{RT}{b} \varphi_{(Red)ir}$  where b is the Tafel slopes and  $\varphi_{(Red)ir}$  is the irreversible potential obtained from the CV curves (see details in Supplementary Materials) [53]. To obtain the Tafel slopes b, two linear sweep voltammetry curves (LSV) were obtained from the CV profiles for each reaction peak (Figure 3b,c). Then, the Tafel slopes were derived by converting the LSV curves into the form of  $E = b \log i + c$  where the E is the voltage and i is the exchange current density [54]. As shown in Figure 3e,f, H-VO<sub>2</sub>@N-CBC exhibits the lowest Tafel slopes in both cathodic peaks (55.76 and 66.74 mV dec<sup>-1</sup>) compared to VO<sub>2</sub>@N-CBC (62.24 and 113.66 mV  $dec^{-1}$ ) as well as N-CBC (74.63 and 163.75 mV  $dec^{-1}$ ). The lowest Tafel slope typically indicates the fastest redox kinetics [55]. Therefore, the difference in activation energy (Ea) in each cathode during the discharge process was estimated (Figure 3d). In the S<sub>8</sub> to LiPSs conversion reaction, the Ea of N-CBC is 16.45 kJ mol<sup>-1</sup> higher than that of  $VO_2@N$ -CBC, while the latter is 11.73 kJ mol<sup>-1</sup> higher than that of H-VO<sub>2</sub>@N-CBC. When soluble LiPSs are converted to solid Li<sub>2</sub>S, H-VO<sub>2</sub>@N-CBC still features the lowest activation energy, which is 28.74 kJ mol<sup>-1</sup> lower than that of VO<sub>2</sub>@N-CBC and 43.34 kJ mol<sup>-1</sup> lower

Batteries 2023, 9, 14 8 of 13

than that of the N-CBC electrode. The lowest activation energy barrier in both reaction steps indicates the best catalytic capability of  $\text{H-VO}_2@\text{N-CBC}$  among these three sulfur hosts [56].

#### 3.4. Charge Transportation Evaluation

To further evaluate the charge transport characteristics, we measured the CVs of these cells with different scan rates ranging from 0.2 to 0.5 mV s<sup>-1</sup>. Upon increasing the scan rate, the anodic and cathodic peaks shifted positively and negatively, leading to a larger polarization (Figure 4a-c). The anodic and cathodic current peaks (I<sub>A</sub>, I<sub>C1</sub>, I<sub>C2</sub>) of all three electrodes feature a linear relationship with the square root of the scanning rates (Figure 4d-f), indicating that the ion diffusion process is the rate-determined step in these electrochemical reactions [57]. The lithium-ion diffusion coefficient (D) was derived using the Randles-Sevcik equation [58]  $I_P = 2.69 \times 10^5 n^{3/2} A \cdot C \cdot D^{1/2} v^{1/2}$  where  $I_P$  is the peak current, *n* is the number of electrons in the reaction, *A* is the electrode area, *C* is the lithium-ion concentration in the electrolyte, and v is the scan rate. The slopes can be derived from the linear relationship between the peak current  $I_P$  and  $v^{1/2}$  at each redox peak. H-VO<sub>2</sub>@N-CBC depicted considerably steeper  $I_P/v^{1/2}$  slopes for each redox reaction when compared with VO<sub>2</sub>@N-CBC and N-CBC, which suggests that H-VO<sub>2</sub>@N-CBC possess the highest lithium-ion diffusion coefficient. The higher slopes of VO<sub>2</sub>@N-CBC than N-CBC imply that the VO<sub>2</sub> NPs are conducive to lithium-ion diffusion. The 3D porous framework as well as the formation of oxygen vacancies in H-VO<sub>2</sub>@N-CBC provide an efficient Li<sup>+</sup>-ions/electrons conduction pathway, which consequently facilitates more rapid charge transportation.

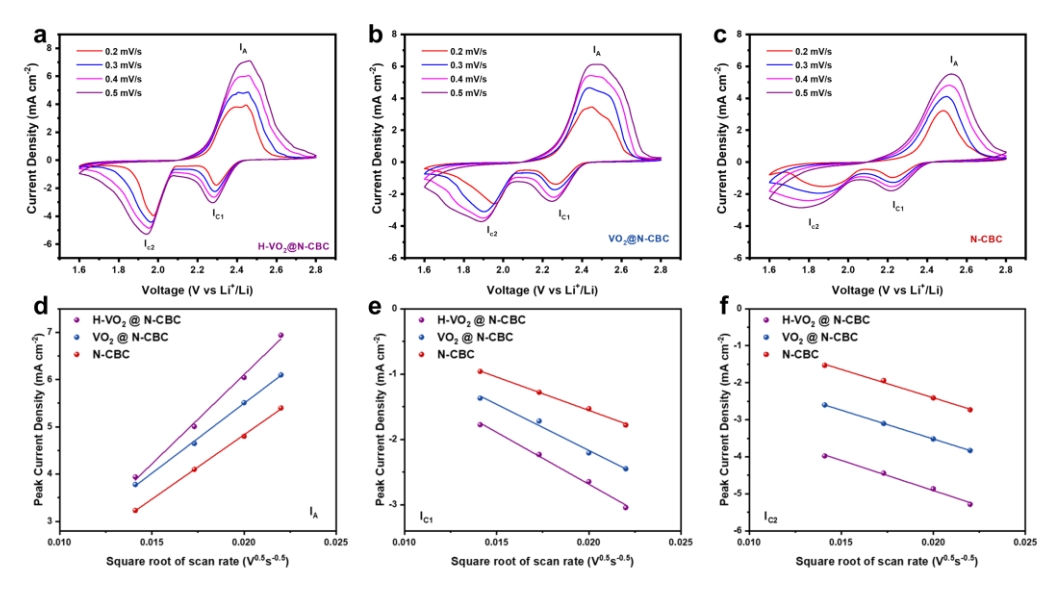


**Figure 4.** Cyclic voltammetry (CV) profiles of Li-S full cells with (a) H-VO<sub>2</sub>@N-CBC, (b) VO<sub>2</sub>@N-CBC, and (c) N-CBC obtained at scan rates from 0.2 to 0.5 mV/s; (d–f) peak current density ( $I_p$ ) versus square root of scan rates ( $v^{0.5}$ ) with three different electrodes at redox peak A, C<sub>1</sub>, and C<sub>2</sub>.

## 3.5. Li-S Battery Performance

Figure 5a–c displays the galvanostatic charge/discharge profiles of the H-VO<sub>2</sub>@N-CBC-, VO<sub>2</sub>@N-CBC- and N-CBC-based sulfur cathodes evaluated by stepwise increasing the rate to 0.1 C, 0.2 C, 0.3 C, 0.5 C and 1 C. When increasing the current density, the charge–discharge curves of H-VO<sub>2</sub>@N-CBC show a smaller polarization shift than those of VO<sub>2</sub>@N-CBC and N-CBC, implying the enhanced kinetics of the conversion reaction with the H-VO<sub>2</sub>@N-CBC cathode materials, which exhibit well-defined dual plateaus even at a high rate of 1 C. Figure 5d shows the overall rate performance of the three types of cathodes from 0.1 to 1 C per every 5 cycles and finally returning to 0.5 C. When cycled at rates of 0.1 C, 0.2 C, 0.3 C, 0.5 C and 1 C, the H-VO<sub>2</sub>@N-CBC/S cathode delivers the highest

Batteries 2023, 9, 14 9 of 13

discharge capacities of 1347, 1123, 1085, 1044 and 957 mA h g $^{-1}$ , respectively. When the current density returns to 0.5 C, it restores a reversible discharge capacity of 1028 mA h g $^{-1}$ , demonstrating the superior electrochemical performance of the H-VO<sub>2</sub>@N-CBC cathode at varying rates.

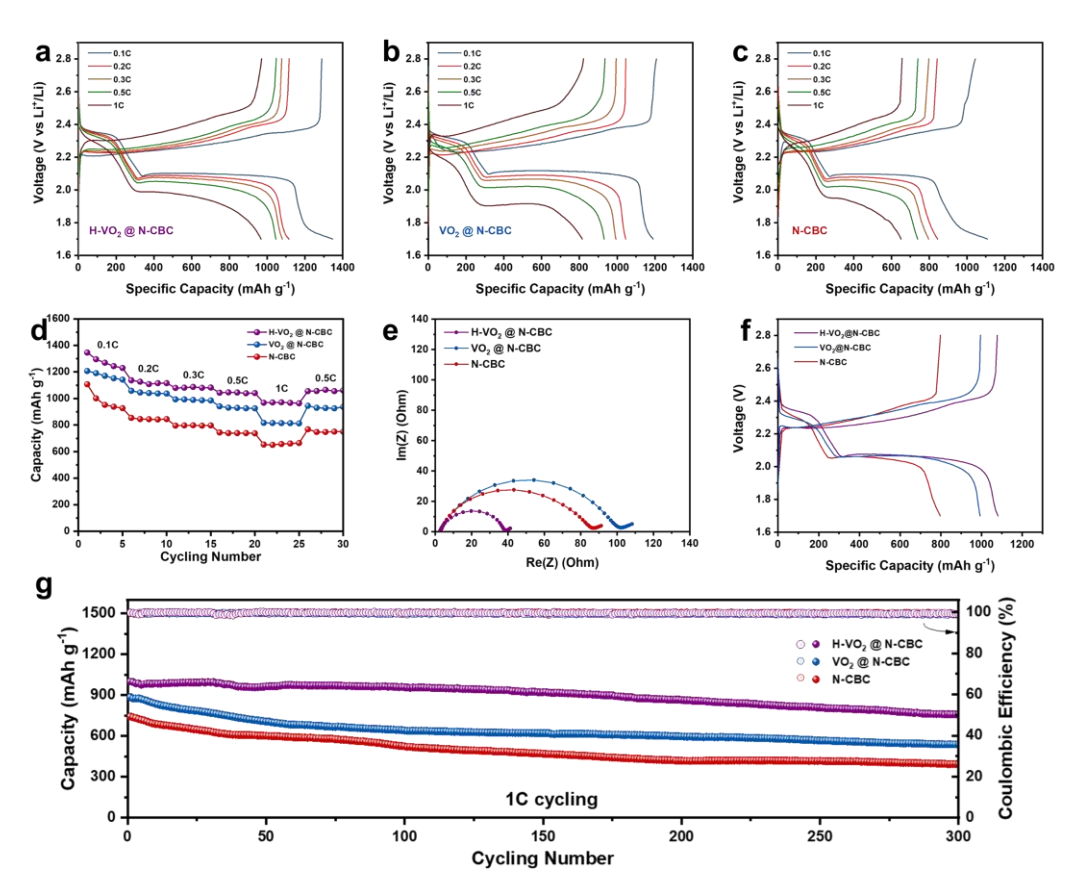


**Figure 5.** Galvanostatic charge / discharge profiles of (a) H-VO<sub>2</sub>@N-CBC-, (b) VO<sub>2</sub>@N-CBC-, and (c) N-CBC-based cathodes at current rates of 0.1, 0.2, 0.3, 0.5, and 1 C; (d) rate performance comparison from 0.1 to 1 C and (e) EIS curves comparison; (f) charge/discharge voltage profile comparison at 0.3 C; (g) long-term cycling stability comparison at 1 C.

The electrochemical impedance spectroscopy (EIS) curves of the H-VO<sub>2</sub>@N-CBC, VO<sub>2</sub>@N-CBC, and N-CBC cathodes were collected, as shown in Figure 5e. The highfrequency semicircles in the Nyquist plots correspond to the charge-transfer resistance (Rct) within the cathodes [59]. The H-VO<sub>2</sub>@N-CBC, VO<sub>2</sub>@N-CBC, and N-CBC cathodes exhibit  $R_{ct}$  values of 36, 84 and 98  $\Omega$ , respectively, which indicates that even though the addition of VO<sub>2</sub> results in a lower electron conductivity due to its intrinsic insulating property, hydrogen thermal treatment can significantly reduce the electrical resistance of VO<sub>2</sub>. The apparently reduced charge-transfer resistance validates the improved reaction kinetics and rate capabilities, which are consistent with the observations in Figure 5a-d. As shown in Figure 5f, the cathode based on H-VO<sub>2</sub>@N-CBC exhibits minimal polarization compared to those based on VO<sub>2</sub>@N-CBC and N-CBC, which can be attributed to less ohmic polarization than VO<sub>2</sub>@N-CBC and a lower activation polarization compared to N-CBC. The longer and flatter lower plateau (Q<sub>L</sub>) during the discharge process suggests that H-VO<sub>2</sub>@N-CBC has a better affinity/absorption for LiPSs than N-CBC and improved conductivity of VO<sub>2</sub> after hydrogen treatment to enable the effective participation of LiPSs in further conversion reactions after chemical capturing [60]. Figure 5g displays the cycling performance of the three cathodes at 1 C. After 300 cycles, the H-VO<sub>2</sub>@N-CBC cathode retains a remarkable discharge capacity of 758 mA h  $g^{-1}$  with a capacity decay of 0.139% per cycle. In contrast, the VO<sub>2</sub>@N-CBC and N-CBC cathodes after 300 cycles deliver

Batteries 2023, 9, 14 10 of 13

capacities of 621 and 457 mA h  $\rm g^{-1}$ , respectively, owing to their inferior ability in catalyzing LiPS conversion. The outstanding electrochemical performance of H-VO<sub>2</sub>@N-CBC reveals enhanced polysulfide redox kinetics, which exploits the intrinsic merits of transition metal oxide while addressing its insulating drawbacks, enabling the synchronous capturing and accelerated conversion of LiPSs. In Table S1 in the Supplementary Materials, we compare our device performance with other recent works on catalysts used in Li-S batteries. Our battery cell exhibits a better rate capability as well as cycling stability at a relatively high sulfur loading.

## 3.6. Catalyst Stability

To observe the catalyst stability, the cells after 300 charge/discharge cycles were disassembled at the fully discharged status. The S-cathode morphology was observed using SEM imaging. With the assistance of H-VO<sub>2</sub> (Figure 6a,b) and VO<sub>2</sub> (Figure 6c,d) NP catalysts, the precipitation of Li<sub>2</sub>S was regulated, and fine Li<sub>2</sub>S particles were uniformly deposited along the surface of the carbon nanofibers. In contrast, without oxide catalysts, bulky Li<sub>2</sub>S clusters (Figure 6c,f) are found in the N-CBC matrix. After 300 cycles, although some Li<sub>2</sub>S agglomerations were observed in the H-VO<sub>2</sub>@N-CBC- and VO<sub>2</sub>@N-CBC-based sulfur electrodes, the Li<sub>2</sub>S reduction products were still firmly immobilized and well-dispersed on the carbon nanofibers, which suggests that the active VO<sub>2</sub> and H-VO<sub>2</sub> NPs were retained on the carbon nanofibers and verified the catalysts' stability during battery cycling. It is worth noting that some Li<sub>2</sub>S clusters were formed in VO<sub>2</sub>@N-CBC in Figure 6e that were not observed in the H-VO<sub>2</sub>@N-CBC matrix. Therefore, H-VO<sub>2</sub> NPs provide a better catalytic ability for converting LiPSs and regulating Li<sub>2</sub>S deposition than VO<sub>2</sub> NPs.

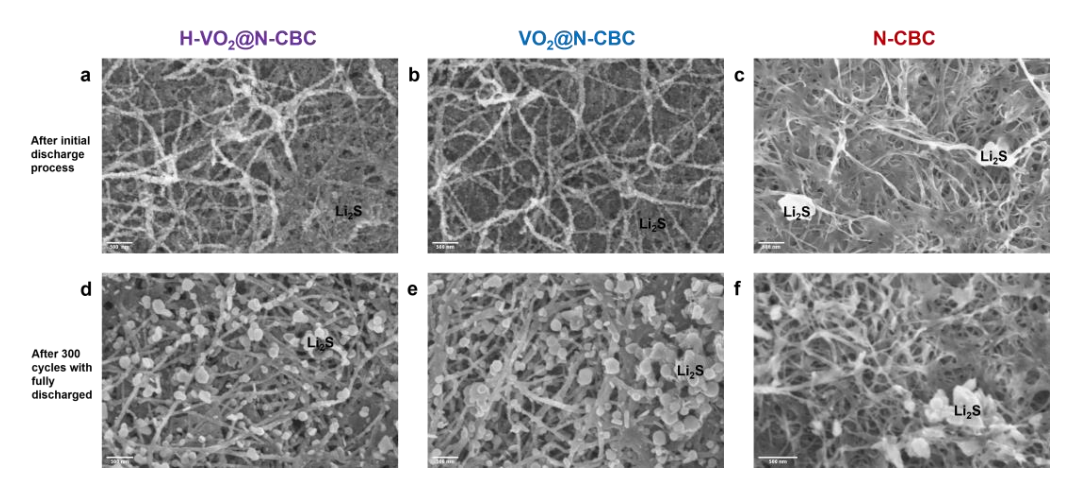


**Figure 6.** SEM images of (a,d) H-VO<sub>2</sub>@N-CBC-, (b,e) VO<sub>2</sub>@N-CBC- and (c,f) N-CBC-based sulfur cathodes at the fully discharged state after initial and 300 cycles.

# 4. Conclusions

In summary, a freestanding composite structure with catalytic H-VO $_2$  NPs anchored on the N-doped CBC scaffold was designed and fabricated as a sulfur host for Li-S batteries. The hydrogen treatment stabilizes the rutile VO $_2$ (R) phase at room temperature and partially reduces it to V $_2$ O $_3$ . Converting the initial insulating VO $_2$ (M) phase into metallic conductive VO $_2$ (R)/V $_2$ O $_3$  improves the cathode's overall conductivity and overcomes the inherent insulating limitation of conventional transition metal oxide catalysts. This change boosts the redox conversion rates of polysulfides, demonstrated by the various electrochemical measurements. Accompanied by the merits of N-doped CBC, the sulfur cathode based on the H-VO $_2$ @N-CBC scaffold delivers a high initial specific capacity of 1347 mAh g $^{-1}$  at 0.1 C and remarkable cycling stability with a capacity of 758 mAh g $^{-1}$  after 300 cycles at 1 C. This work provides an effective strategy to design and fabricate conductive catalysts from a typical transition metal oxide (VO $_2$ ) and subsequently promotes the electrochemical performance of Li-S batteries.

Batteries 2023, 9, 14 11 of 13

**Supplementary Materials:** The following supporting information can be downloaded at: https://www.mdpi.com/article/10.3390/batteries9010014/s1, Figure S1: The CV curves of H-VO<sub>2</sub>@N-CBC-, VO<sub>2</sub>@N-CBC- and N-CBC-based electrodes in a symmetric cell with Li2S6 as the electrolyte at the scan rate of 3 mV/s. The redox peaks are labeled as a, b, c, and d, respectively; Table S1: Comparison of the electrochemical performance of LSBs using different catalytic materials. References [61–65] are cited in the supplementary materials.

**Author Contributions:** Conceptualization, X.L. and Z.F.; methodology, X.L., W.L. and Z.F.; investigation, X.L.; resources, S.W. and Z.F.; writing—original draft preparation, X.L.; writing—review and editing, X.P., S.W. and Z.F.; supervision, Z.F.; funding acquisition, S.W. and Z.F. All authors have read and agreed to the published version of the manuscript.

**Funding:** This research was funded by the National Science Foundation of USA, grant number 2129983 and 2103582.

**Data Availability Statement:** Not applicable.

**Conflicts of Interest:** The authors declare no conflict of interest.

#### References

Manthiram, A.; Fu, Y.; Su, Y.-S. Challenges and Prospects of Lithium–Sulfur Batteries. Acc. Chem. Res. 2013, 46, 1125–1134.
 [CrossRef] [PubMed]

- 2. Yang, Y.; Zheng, G.; Cui, Y. Nanostructured sulfur cathodes. Chem. Soc. Rev. 2013, 42, 3018–3032. [CrossRef] [PubMed]
- 3. Rehman, S.; Tang, T.; Ali, Z.; Huang, X.; Hou, Y.J.S. Integrated design of MnO<sub>2</sub>@ carbon hollow nanoboxes to synergistically encapsulate polysulfides for empowering lithium sulfur batteries. *Small* **2017**, *13*, 1700087. [CrossRef] [PubMed]
- 4. Gueon, D.; Ju, M.-Y.; Moon, J.H. Complete encapsulation of sulfur through interfacial energy control of sulfur solutions for high-performance Li-S batteries. *Proc. Natl. Acad. Sci. USA* **2020**, *117*, 12686–12692. [CrossRef] [PubMed]
- 5. Xi, K.; Kidambi, P.R.; Chen, R.; Gao, C.; Peng, X.; Ducati, C.; Hofmann, S.; Kumar, R.V. Binder free three-dimensional sulphur/few-layer graphene foam cathode with enhanced high-rate capability for rechargeable lithium sulphur batteries. *Nanoscale* **2014**, *6*, 5746–5753. [CrossRef]
- 6. Zheng, M.; Chi, Y.; Hu, Q.; Tang, H.; Jiang, X.; Zhang, L.; Zhang, S.; Pang, H.; Xu, Q. Carbon nanotube-based materials for lithium–sulfur batteries. *J. Mater. Chem. A* **2019**, *7*, 17204–17241. [CrossRef]
- 7. Doñoro, Á.; Muñoz-Mauricio, Á.; Etacheri, V. High-Performance Lithium Sulfur Batteries Based on Multidimensional Graphene-CNT-Nanosulfur Hybrid Cathodes. *Batteries* **2021**, *7*, 26. [CrossRef]
- 8. Li, S.; Mou, T.; Ren, G.; Warzywoda, J.; Wang, B.; Fan, Z. Confining Sulfur Species in Cathodes of Lithium–Sulfur Batteries: Insight into Nonpolar and Polar Matrix Surfaces. *ACS Energy Lett.* **2016**, *1*, 481–489. [CrossRef]
- 9. Pei, F.; An, T.; Zang, J.; Zhao, X.; Fang, X.; Zheng, M.; Dong, Q.; Zheng, N. From Hollow Carbon Spheres to N-Doped Hollow Porous Carbon Bowls: Rational Design of Hollow Carbon Host for Li-S Batteries. *Adv. Energy Mater.* **2016**, *6*, 1502539. [CrossRef]
- 10. Chen, M.; Zhao, S.; Jiang, S.; Huang, C.; Wang, X.; Yang, Z.; Xiang, K.; Zhang, Y. Suppressing the Polysulfide Shuttle Effect by Heteroatom-Doping for High-Performance Lithium–Sulfur Batteries. *ACS Sustain. Chem. Eng.* **2018**, *6*, 7545–7557. [CrossRef]
- 11. Li, N.; Yu, L.; Yang, J.; Zheng, B.; Qiu, X.; Xi, J. Identifying the active sites and multifunctional effects in nitrogen-doped carbon microtube interlayer for confining-trapping-catalyzing polysulfides. *Nano Energy* **2021**, *79*, 105466. [CrossRef]
- 12. Laverde, J.; Rosero-Navarro, N.C.; Miura, A.; Buitrago-Sierra, R.; Tadanaga, K.; López, D. Impact of Sulfur Infiltration Time and Its Content in an N-doped Mesoporous Carbon for Application in Li-S Batteries. *Batteries* **2022**, *8*, 58. [CrossRef]
- 13. Waluś, S.; Barchasz, C.; Bouchet, R.; Leprêtre, J.-C.; Colin, J.-F.; Martin, J.-F.; Elkaïm, E.; Baehtz, C.; Alloin, F. Lithium/Sulfur Batteries Upon Cycling: Structural Modifications and Species Quantification by In Situ and Operando X-Ray Diffraction Spectroscopy. *Adv. Energy Mater.* **2015**, *5*, 1500165. [CrossRef]
- Lang, X.; Zhao, Y.; Cai, K.; Li, L.; Chen, D.; Zhang, Q. A facile synthesis of stable TiO<sub>2</sub>/TiC composite material as sulfur immobilizers for cathodes of lithium–sulfur batteries with excellent electrochemical performances. *Energy Technol.* 2019, 7, 1900543. [CrossRef]
- 15. Guo, Y.; Zhang, Y.; Xiang, M.; Wu, H.; Liu, H.; Dou, S. Interwoven V<sub>2</sub>O<sub>5</sub> nanowire/graphene nanoscroll hybrid assembled as efficient polysulfide-trapping-conversion interlayer for long-life lithium–sulfur batteries. *J. Mater. Chem. A* **2018**, *6*, 19358–19370. [CrossRef]
- 16. Xu, J.; Zhang, W.; Fan, H.; Cheng, F.; Su, D.; Wang, G. Promoting lithium polysulfide/sulfide redox kinetics by the catalyzing of zinc sulfide for high performance lithium-sulfur battery. *Nano Energy* **2018**, *51*, 73–82. [CrossRef]
- 17. Wang, S.; Chen, H.; Liao, J.; Sun, Q.; Zhao, F.; Luo, J.; Lin, X.; Niu, X.; Wu, M.; Li, R.; et al. Efficient trapping and catalytic conversion of polysulfides by VS<sub>4</sub> nanosites for Li–S batteries. *ACS Energy Lett.* **2019**, *4*, 755–762. [CrossRef]
- 18. Cho, J.; Ryu, S.; Gong, Y.J.; Pyo, S.; Yun, H.; Kim, H.; Lee, J.; Yoo, J.; Kim, Y.S. Nitrogen-doped MoS<sub>2</sub> as a catalytic sulfur host for lithium-sulfur batteries. *Chem. Eng. J.* **2022**, *439*, 135568. [CrossRef]

Batteries 2023, 9, 14 12 of 13

19. Li, W.; Li, S.; Bernussi, A.A.; Fan, Z. 3-D edge-oriented electrocatalytic NiCo<sub>2</sub>S<sub>4</sub> nanoflakes on vertical graphene for Li-S batteries. *Energy Mater. Adv.* **2021**, 2021, 2712391.

- 20. Wang, S.; Feng, S.; Liang, J.; Su, Q.; Zhao, F.; Song, H.; Zheng, M.; Sun, Q.; Song, Z.; Jia, X.; et al. Insight into MoS<sub>2</sub>–MoN Heterostructure to Accelerate Polysulfide Conversion toward High-Energy-Density Lithium–Sulfur Batteries. *Adv. Energy Mater.* **2021**, *11*, 2003314.
- 21. He, J.; Chen, Y.; Manthiram, A. Vertical Co9S8 hollow nanowall arrays grown on a Celgard separator as a multifunctional polysulfide barrier for high-performance Li–S batteries. *Energy Environ. Sci.* **2018**, *11*, 2560–2568.
- 22. Lim, W.-G.; Kim, S.; Jo, C.; Lee, J. A Comprehensive Review of Materials with Catalytic Effects in Li–S Batteries: Enhanced Redox Kinetics. *Angew. Chem.* **2019**, *58*, 18746–18757. [CrossRef] [PubMed]
- 23. Liu, X.; Huang, J.Q.; Zhang, Q.; Mai, L. Nanostructured metal oxides and sulfides for lithium–sulfur batteries. *Adv. Mater.* **2017**, 29, 1601759. [CrossRef]
- 24. Zhang, B.; Luo, C.; Deng, Y.; Huang, Z.; Zhou, G.; Lv, W.; He, Y.B.; Wan, Y.; Kang, F.; Yang, Q.-H. Optimized catalytic WS<sub>2</sub>–WO<sub>3</sub> heterostructure design for accelerated polysulfide conversion in lithium–sulfur batteries. *Adv. Energy Mater.* **2020**, *10*, 2000091. [CrossRef]
- 25. Liang, Z.; Zheng, G.; Li, W.; Seh, Z.W.; Yao, H.; Yan, K.; Kong, D.; Cui, Y. Sulfur Cathodes with Hydrogen Reduced Titanium Dioxide Inverse Opal Structure. *ACS Nano* **2014**, *8*, 5249–5256.
- 26. Pang, Q.; Kundu, D.; Cuisinier, M.; Nazar, L.F. Surface-enhanced redox chemistry of polysulphides on a metallic and polar host for lithium-sulphur batteries. *Nat. Commun.* **2014**, *5*, 4759. [CrossRef] [PubMed]
- 27. Zhang, H.; Ono, L.K.; Tong, G.; Liu, Y.; Qi, Y. Long-life lithium-sulfur batteries with high areal capacity based on coaxial CNTs@TiN-TiO<sub>2</sub> sponge. *Nat. Commun.* **2021**, *12*, 4738. [CrossRef]
- 28. Zhao, Y.; Lee, J.H.; Zhu, Y.; Nazari, M.; Chen, C.; Wang, H.; Bernussi, A.; Holtz, M.; Fan, Z. Structural, electrical, and terahertz transmission properties of VO<sub>2</sub> thin films grown on c-, r-, and m-plane sapphire substrates. *J. Appl. Phys.* **2012**, *111*, 053533.
- 29. Zhao, Y.; Karaoglan-Bebek, G.; Pan, X.; Holtz, M.; Bernussi, A.A.; Fan, Z. Hydrogen-doping stabilized metallic VO<sub>2</sub> (R) thin films and their application to suppress Fabry-Perot resonances in the terahertz regime. *Appl. Phys. Lett.* **2014**, *104*, 241901. [CrossRef]
- 30. Wu, C.; Feng, F.; Feng, J.; Dai, J.; Peng, L.; Zhao, J.; Yang, J.; Si, C.; Wu, Z.; Xie, Y. Hydrogen-Incorporation Stabilization of Metallic VO<sub>2</sub>(R) Phase to Room Temperature, Displaying Promising Low-Temperature Thermoelectric Effect. *J. Am. Chem. Soc.* **2011**, *133*, 13798–13801. [CrossRef]
- 31. Fan, L.; Zhu, Y.; Zhao, S.; Wang, Z.; Liu, Z.; Zhu, L.; Wang, B.; Zhang, Q. Modulation of VO<sub>2</sub> metal-insulator transition by co-doping of hydrogen and oxygen vacancy. *Sol. Energy Mater. Sol. Cells* **2020**, 212, 110562. [CrossRef]
- 32. Wei, J.; Ji, H.; Guo, W.; Nevidomskyy, A.H.; Natelson, D. Hydrogen stabilization of metallic vanadium dioxide in single-crystal nanobeams. *Nat. Nanotechnol.* **2012**, *7*, 357–362. [CrossRef]
- 33. Pan, X.; Ren, G.; Hoque, M.N.F.; Bayne, S.; Zhu, K.; Fan, Z. Fast Supercapacitors Based on Graphene-Bridged V<sub>2</sub>O<sub>3</sub>/VOx Core–Shell Nanostructure Electrodes with a Power Density of 1 MW kg<sup>-1</sup>. *Adv. Mater. Interfaces* **2014**, *1*, 1400398. [CrossRef]
- 34. Li, S.; Mou, T.; Ren, G.; Warzywoda, J.; Wei, Z.; Wang, B.; Fan, Z. Gel based sulfur cathodes with a high sulfur content and large mass loading for high-performance lithium–sulfur batteries. *J. Mater. Chem. A* **2017**, *5*, 1650–1657. [CrossRef]
- 35. Robinson, J.B.; Xi, K.; Kumar, R.V.; Ferrari, A.C.; Au, H.; Titirici, M.-M.; Parra-Puerto, A.; Kucernak, A.; Fitch, S.D.; Garcia-Araez, N.; et al. 2021 roadmap on lithium sulfur batteries. *J. Phys. Energy* **2021**, *3*, 031501. [CrossRef]
- 36. Wang, J.; Han, W.-Q. A Review of Heteroatom Doped Materials for Advanced Lithium–Sulfur Batteries. *Adv. Funct. Mater.* **2022**, 32, 2107166. [CrossRef]
- 37. Huang, Y.; Lin, Z.; Zheng, M.; Wang, T.; Yang, J.; Yuan, F.; Lu, X.; Liu, L.; Sun, D. Amorphous Fe<sub>2</sub>O<sub>3</sub> nanoshells coated on carbonized bacterial cellulose nanofibers as a flexible anode for high-performance lithium ion batteries. *J. Power Sources* **2016**, 307, 649–656. [CrossRef]
- 38. Zheng, J.; Zhang, Y.; Meng, C.; Wang, X.; Liu, C.; Bo, M.; Pei, X.; Wei, Y.; Lv, T.; Cao, G. V<sub>2</sub>O<sub>3</sub>/C nanocomposites with interface defects for enhanced intercalation pseudocapacitance. *Electrochim. Acta* **2019**, *318*, 635–643. [CrossRef]
- 39. Arteaga-Cardona, F.; Franco-Bacca, A.P.; Cervantes-Alvarez, F.; Alvarado-Gil, J.J.; Silva-González, N.R.; Salazar-Kuri, U. Simple thermal decomposition synthesis of monoclinic VO<sub>2</sub>. *Appl. Phys. A* **2021**, 127, 159. [CrossRef]
- 40. Zhang, J.; Zhao, Z.; Li, J.; Jin, H.; Rehman, F.; Chen, P.; Jiang, Y.; Chen, C.; Cao, M.; Zhao, Y. Evolution of Structural and Electrical Properties of Oxygen-Deficient VO<sub>2</sub> under Low Temperature Heating Process. ACS Appl. Mater. Interfaces 2017, 9, 27135–27141. [CrossRef]
- 41. Ning, Y.; Wang, B.; Jin, F.; Yang, J.; Zhang, J.; Luo, H.; Wu, F.; Zhang, Z.; Zhang, H.; Zhou, Y.; et al. A rational VO<sub>2</sub> nan-otube/graphene binary sulfur host for superior lithium-sulfur batteries. *J. Alloy. Compd.* **2020**, *838*, 155504. [CrossRef]
- 42. Zhao, J.; Zhao, Y.; Yue, W.-C.; Li, X.; Gao, N.; Zhang, Y.-J.; Hu, C.-Q. V<sub>2</sub>O<sub>3</sub>/VN Catalysts Decorated Free-Standing Multifunctional Interlayer for High-Performance Li-S Battery. *Chem. Eng. J.* **2022**, 441, 136082. [CrossRef]
- 43. Lai, Q.; Zheng, L.; Liang, Y.; He, J.; Zhao, J.; Chen, J. Metal-Organic-Framework-Derived Fe-N/C Electrocatalyst with Five-Coordinated Fe-Nx Sites for Advanced Oxygen Reduction in Acid Media. *ACS Catal.* **2017**, *7*, 1655–1663. [CrossRef]
- 44. Fedoseeva, Y.V.; Shlyakhova, E.V.; Stolyarova, S.G.; Vorfolomeeva, A.A.; Grebenkina, M.A.; Makarova, A.A.; Shubin, Y.V.; Okotrub, A.V.; Bulusheva, L.G. Brominated Porous Nitrogen-Doped Carbon Materials for Sodium-Ion Storage. *Batteries* **2022**, *8*, 114. [CrossRef]

Batteries 2023, 9, 14 13 of 13

45. Liang, B.; Zhao, Y.; Zong, M.; Huo, S.; Khan, I.U.; Li, K.; Lv, C. Hierarchically porous N-doped carbon encapsulating CoO/MgO as superior cathode catalyst for microbial fuel cell. *Chem. Eng. J.* **2020**, *385*, 123861. [CrossRef]

- 46. Gao, Y.; Hu, G.; Zhong, J.; Shi, Z.; Zhu, Y.; Su, D.S.; Wang, J.; Bao, X.; Ma, D. Nitrogen-Doped sp2-Hybridized Carbon as a Superior Catalyst for Selective Oxidation. *Angew. Chem. Int. Ed.* **2013**, 52, 2109–2113. [CrossRef]
- 47. Liang, X.; Kwok, C.Y.; Lodi-Marzano, F.; Pang, Q.; Cuisinier, M.; Huang, H.; Hart, C.J.; Houtarde, D.; Kaup, K.; Sommer, H.; et al. Tuning Transition Metal Oxide–Sulfur Interactions for Long Life Lithium Sulfur Batteries: The "Goldilocks" Principle. *Adv. Energy Mater.* **2016**, *6*, 1501636. [CrossRef]
- 48. Zhang, J.; You, C.; Lin, H.; Wang, J. Electrochemical Kinetic Modulators in Lithium–Sulfur Batteries: From Defect-Rich Catalysts to Single Atomic Catalysts. *Energy Environ. Mater.* **2022**, *5*, 731–750. [CrossRef]
- 49. Zhou, J.; Liu, X.; Zhu, L.; Zhou, J.; Guan, Y.; Chen, L.; Niu, S.; Cai, J.; Sun, D.; Zhu, Y.; et al. Deciphering the Modulation Essence of p Bands in Co-Based Compounds on Li-S Chemistry. *Joule* 2018, 2, 2681–2693. [CrossRef]
- 50. Li, Z.; Zhou, Y.; Wang, Y.; Lu, Y.-C. Solvent-Mediated Li<sub>2</sub>S Electrodeposition: A Critical Manipulator in Lithium–Sulfur Batteries. *Adv. Energy Mater.* **2019**, *9*, 1802207. [CrossRef]
- 51. Fan, F.Y.; Carter, W.C.; Chiang, Y.M. Mechanism and kinetics of Li<sub>2</sub>S precipitation in lithium–sulfur batteries. *Adv. Mater.* **2015**, 27, 5203–5209. [CrossRef] [PubMed]
- 52. Huang, X.; Wang, Z.; Knibbe, R.; Luo, B.; Ahad, S.A.; Sun, D.; Wang, L. Cyclic voltammetry in lithium–sulfur batteries—Challenges and opportunities. *Energy Technol.* **2019**, *7*, 1801001. [CrossRef]
- 53. Hua, W.; Li, H.; Pei, C.; Xia, J.; Sun, Y.; Zhang, C.; Lv, W.; Tao, Y.; Jiao, Y.; Zhang, B.; et al. Selective Catalysis Remedies Polysulfide Shuttling in Lithium-Sulfur Batteries. *Adv. Mater.* **2021**, *33*, 2101006. [CrossRef] [PubMed]
- 54. Jing, E.; Chen, L.; Xu, S.; Tian, W.; Zhang, D.; Wang, N.; Bai, Z.; Zhou, X.; Liu, S.; Duan, D.; et al. Dual redox catalysis of VN/nitrogen-doped graphene nanocomposites for high-performance lithium-sulfur batteries. *J. Energy Chem.* **2022**, *64*, 574–582. [CrossRef]
- 55. Sun, Z.; Vijay, S.; Heenen, H.H.; Eng, A.Y.S.; Tu, W.; Zhao, Y.; Koh, S.W.; Gao, P.; Seh, Z.W.; Chan, K.; et al. Catalytic Polysulfide Conversion and Physiochemical Confinement for Lithium–Sulfur Batteries. *Adv. Energy Mater.* **2020**, *10*, 1904010. [CrossRef]
- 56. Luo, C.; Liang, X.; Sun, Y.; Lv, W.; Sun, Y.; Lu, Z.; Hua, W.; Yang, H.; Wang, R.; Yan, C.; et al. An organic nickel salt-based electrolyte additive boosts homogeneous catalysis for lithium-sulfur batteries. *Energy Storage Mater.* **2020**, *33*, 290–297. [CrossRef]
- 57. Zhou, G.; Tian, H.; Jin, Y.; Tao, X.; Liu, B.; Zhang, R.; Seh, Z.W.; Zhuo, D.; Liu, Y.; Sun, J.; et al. Catalytic oxidation of Li<sub>2</sub>S on the surface of metal sulfides for Li-S batteries. *Proc. Natl. Acad. Sci. USA* **2017**, 114, 840–845. [CrossRef]
- 58. Lei, T.; Chen, W.; Lv, W.; Huang, J.; Zhu, J.; Chu, J.; Yan, C.; Wu, C.; Yan, Y.; He, W.; et al. Inhibiting Polysulfide Shuttling with a Graphene Composite Separator for Highly Robust Lithium-Sulfur Batteries. *Joule* **2018**, *2*, 2091–2104. [CrossRef]
- 59. Waluś, S.; Barchasz, C.; Bouchet, R.; Alloin, F. Electrochemical impedance spectroscopy study of lithium–sulfur batteries: Useful technique to reveal the Li/S electrochemical mechanism. *Electrochim. Acta* **2020**, 359, 136944. [CrossRef]
- 60. Zhou, L.; Li, H.; Wu, X.; Zhang, Y.; Danilov, D.L.; Eichel, R.-A.; Notten, P.H.L. Double-Shelled Co<sub>3</sub>O<sub>4</sub>/C Nanocages Enabling Polysulfides Adsorption for High-Performance Lithium–Sulfur Batteries. *ACS Appl. Energy Mater.* **2019**, 2, 8153–8162. [CrossRef]
- Li, F.; Zhang, M.; Chen, W.; Cai, X.; Rao, H.; Chang, J.; Fang, Y.; Zhong, X.; Yang, Y.; Yang, Z.; et al. Vanadium Nitride Quantum Dots/Holey Graphene Matrix Boosting Adsorption and Conversion Reaction Kinetics for High-Performance Lithium–Sulfur Batteries. ACS Appl. Mater. Interfaces 2021, 13, 30746–30755. [CrossRef]
- 62. Wang, S.; Liao, J.; Yang, X.; Liang, J.; Sun, Q.; Liang, J.; Zhao, F.; Koo, A.; Kong, F.; Yao, Y.; et al. Designing a highly efficient polysulfide conversion catalyst with paramontroseite for high-performance and long-life lithium-sulfur batteries. *Nano Energy* **2019**, 57, 230–240. [CrossRef]
- 63. Song, Y.; Zhao, W.; Zhu, X.; Zhang, L.; Li, Q.; Ding, F.; Liu, Z.; Sun, J. Vanadium Dioxide-Graphene Composite with Ultrafast Anchoring Behavior of Polysulfides for Lithium–Sulfur Batteries. *ACS Appl. Mater. Interfaces* **2018**, *10*, 15733–15741. [CrossRef] [PubMed]
- 64. Zhou, T.; Lv, W.; Li, J.; Zhou, G.; Zhao, Y.; Fan, S.; Liu, B.; Li, B.; Kang, F.; Yang, Q.-H. Twinborn TiO2–TiN heterostructures enabling smooth trapping–diffusion–conversion of polysulfides towards ultralong life lithium–sulfur batteries. *Energy Environ. Sci.* 2017, 10, 1694–1703. [CrossRef]
- 65. Liang, X.; Hart, C.; Pang, Q.; Garsuch, A.; Weiss, T.; Nazar, L.F. A highly efficient polysulfide mediator for lithium–sulfur batteries. *Nat. Commun.* **2015**, *6*, 5682. [CrossRef]

**Disclaimer/Publisher's Note:** The statements, opinions and data contained in all publications are solely those of the individual author(s) and contributor(s) and not of MDPI and/or the editor(s). MDPI and/or the editor(s) disclaim responsibility for any injury to people or property resulting from any ideas, methods, instructions or products referred to in the content.